

Ferroelectricity in an Antiferromagnetic Vanadium Trichloride Monolayer

Jinghao Deng^{1#}, Deping Guo^{2,3#}, Yao Wen^{1#}, Shuangzan Lu^{1,4#}, Zhengbo Cheng¹, Zemin Pan¹, Tao Jian¹, Yusong Bai¹, Hui Zhang¹, Wei Ji^{2,3*}, Jun He^{1*}, Chendong Zhang^{1*}

¹*School of Physics and Technology, and Key Laboratory of Artificial Micro- and Nano-structures of Ministry of Education, Wuhan University, Wuhan, 430072, China*

²*Beijing Key Laboratory of Optoelectronic Functional Materials & Micro-Nano Devices, Department of Physics, Renmin University of China, Beijing 100872, China*

³*Key Laboratory of Quantum State Construction and Manipulation (Ministry of Education), Renmin University of China, Beijing, 100872, China*

⁴*Hubei Jiufengshan Laboratory, Wuhan, 430074, China*

[#]*These authors contributed equally: Jinghao Deng, Deping Guo, Yao Wen, Shuangzan Lu.*

^{*}*Correspondence author E-mail: wji@ruc.edu.cn (W.J.), He-jun@whu.edu.cn (J.H.), cdzhang@whu.edu.cn (C.D.Z)*

Abstract: Multiferroicity allows magnetism to be controlled using electric fields or vice versa, which has gained tremendous interest in both fundamental research and device applications. A reduced dimensionality of multiferroic materials is highly desired for device miniaturization, but the coexistence of ferroelectricity and magnetism at the two-dimensional limit is still debated. Here, we used a NbSe₂ substrate to break both the C₃ rotational and inversion symmetries in monolayer VCl₃ and thus introduced exceptional in-plane ferroelectricity into a two-dimensional magnet. Scanning tunnelling spectroscopy directly visualized ferroelectric domains and manipulated their domain boundaries in monolayer VCl₃, where coexisting antiferromagnetic order with canted magnetic moments was verified by vibrating sample magnetometer measurements. Our density functional theory calculations highlight the crucial role that highly directional interfacial Cl–Se interactions play in breaking the symmetries and thus in introducing in-plane ferroelectricity, which was further verified by examining an ML-VCl₃/graphene sample. Our work demonstrates an approach to manipulate the ferroelectric states in monolayered magnets through van der Waals interfacial interactions.

Spontaneous polarizations in solid materials, including spin and electric polarizations, are crucial characteristics for functional device applications. This scenario has been extended to studies of two-dimensional van der Waals (2D vdW) materials. In past years, substantial efforts have been made to validate that either magnetic^{1,2} or ferroelectric (FE) order^{3,4} can be preserved at the 2D limit. These findings immediately stimulated the search for vdW monolayers (MLs) to simultaneously combine two (or more) ferroic order parameters, namely, to realize ML multiferroicity (MF). Although quite a few candidate MLs were theoretically predicted to host either type-I^{5,6} or type-II⁷ ML MF, likely experimental evidence of a multiferroic ML was only revealed for the NiI₂ ML based on all-optical methods⁸. However, this result, especially the experimental determination of ferroelectricity, is still in debate⁹⁻¹⁴. In addition to vdW MLs, the coexistence of ferroelectricity and ferromagnetism was reported for a non-vdW crystal (Cr₂S₃) with a single-unit-cell thickness¹⁵ during the preparation of this work.

A promising route towards realizing ML MF lies in introducing electric polarizations into known 2D magnets by artificially engineering spatial symmetries. For instance, Huang *et al.* theoretically proposed that Li intercalation or proper charge doping in ML CrBr₃ can lead to FE order coexisting with ferromagnetism¹⁶. Unlike closed-shell Cr³⁺ ions, open-shell V³⁺ ions enable ML vanadium trihalides (VX₃) to exhibit mutable orbital ordering, which, in principle, makes them a more feasible materials family for tailoring lattice symmetries and thus inducing electric polarizations¹⁷. On the experimental side, bulk forms of VX₃ are known to be magnetic with either ferromagnetic (VI₃)¹⁸⁻²⁰ or antiferromagnetic (VCl₃, VBr₃)²¹⁻²³ configurations. Peculiar

orbital orderings²⁴ and the interplay of magnetic and structural degrees of freedom²⁵ have also been found in their bulk crystals. At the ML limit, however, experimental exploration is rare, with sporadic studies reported for VX₃ MLs²⁵. Therefore, whether magnetism and electric polarization can be simultaneously retained in ML-VX₃ remains unclear.

Here, we epitaxially grow a VCl₃ ML on a NbSe₂ substrate, in which we report experimental identification of the coexistence of ferroelectricity and antiferromagnetism. The in-plane (IP) ferroelectricity in the VCl₃ ML is directly imaged and manipulated using scanning tunnelling microscopy/spectroscopy (STM/S). Multiple findings are examined to verify the ferroelectricity, including severe distortion of the atomic lattice, electric-polarization-induced energy band bending, and tip-induced flipping of the polarization. Moreover, vibrating sample magnetometry (VSM) and density functional theory (DFT) calculations provide consistent evidence that the FE VCl₃ ML hosts a bistriped antiferromagnetic (AFM) order ($T_N=16$ K) with an x - z easy plane for magnetization. Our DFT calculations further corroborate that this magnetic order is selectively stabilized by the NbSe₂ substrate, which gives rise to a distorted geometry resulting in spontaneous breaking of the C_3 rotational symmetry. The broken structural symmetry, promoted by directional interfacial Se–Cl interactions and incomplete electronic screening, leads to appreciable IP total electric polarization. To verify our theory, a control experiment is performed on VCl₃/graphene where IP ferroelectricity is absent. Given these results, this work experimentally realizes, to the

best of our knowledge, the first example of introducing ferroelectricity into a magnetic monolayer via appealing vdW interface engineering.

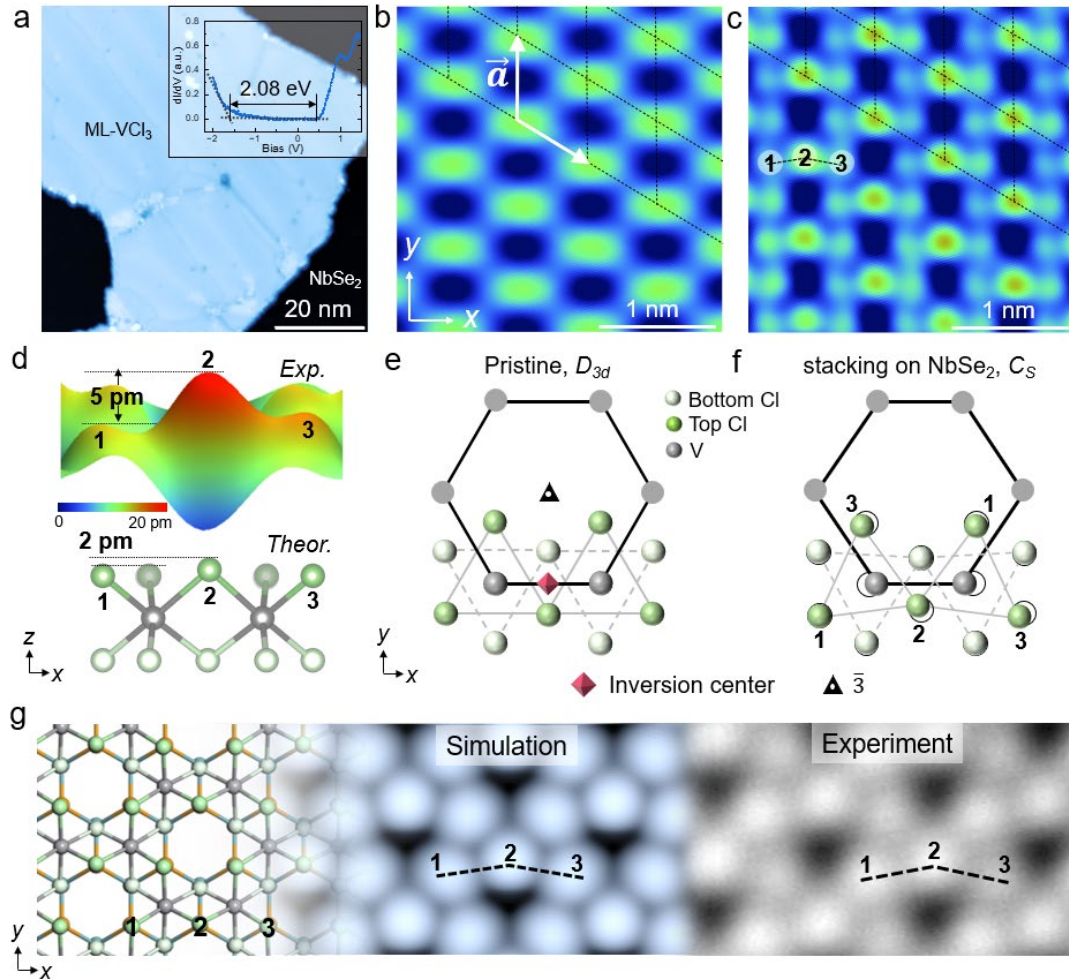


Figure 1 | Morphology and atomic structure of ML-VCl₃ on a NbSe₂ substrate. **a**, Large-scale morphology of an ML-VCl₃ flake grown on a cleaved NbSe₂ surface ($V_b = 1.5$ V, $I_t = 20$ pA, and scale bar: 20 nm). Inset: typical dI/dV spectrum showing a bandgap of 2.08 eV (details in Fig. S2). The feedback loop opened at $V_b = 1.8$ V and $I_t = 300$ pA with lock-in modulation $V_{rms} = 6$ mV. **b**, Zoomed-in STM image of NbSe₂-supported VCl₃, $V_b = 1.5$ V, $I_t = 50$ pA, and scale bar: 1 nm. The dashed black lines indicate the triangular lattice of oval protrusions. The orthometric x - y coordinates are defined with x along the armchair direction of the triangular lattice of the oval protrusions. The white arrow connecting two neighbouring protrusions represents the lattice constant a , as discussed in the main text. **c**, Atomically resolved STM images of the same region as in **b**. $V_b = -0.35$ V, $I_t = 50$ pA, and scale bar: 1 nm. The dashed black lines indicate the triangular lattice shown in **b**. Three inequivalent Cl atoms are marked by numbers 1, 2, and 3 in black (the other numbers coloured black follow the same definitions hereafter). A black boomerang-like polygonal line that connects three Cl atoms is defined. **d**, Three-dimensional STM image zoomed in on a three Cl atom boomerang (upper panel) and a side view of the calculated atomic model (lower panel). The V, top-layer Cl, and bottom-layer Cl atoms are shown in grey, dark green, and bright green, respectively. **e** and **f**, Schematic representation of pristine

VCl₃ and NbSe₂-supported VCl₃, respectively. The NbSe₂ lattice is not displayed for simplicity. The red rhombus and black triangle represent the inversion symmetry and threefold rotational symmetry centers, respectively. **g**, Comparison of the DFT calculation result of the crystalline structure (left panel), the simulated STM image (middle panel), and the experimental STM image (right panel) of NbSe₂-supported VCl₃. The Nb and Se atoms are shown in blue and orange, respectively.

We started our exploration with molecular beam epitaxy (MBE) growth of VCl₃ MLs on freshly cleaved NbSe₂ substrates (see Methods for details). Figure 1a shows a typical STM topography image of an as-grown ML-VCl₃ film exhibiting a thickness of approximately 5.6 Å (Fig. S1). A typical tunnelling conductance spectrum indicates a 2.08 eV bandgap for the ML, supporting the semiconducting electronic structures calculated in the band structure calculations^{17,26} with the electronic correlation and orbital ordering considered (for details, see Fig. S2). In particular, V atoms are arranged in a honeycomb lattice, and each V atom is embedded in an octahedron composed of six Cl atoms. Therefore, an STM topography showing triangular protrusions is expected for VCl₃, akin to those of epitaxial CrBr₃²⁷ and CrI₃²⁸. Each of these triangles reflects three top-layer Cl atoms surrounding a threefold rotational symmetry center of the V atom. However, our STM imaging of the VCl₃ ML shows distinctively different features. Under a relatively large bias, e.g., 1.5 V, the observed protrusions appear as elongated ovals (Fig. 1b). These oval protrusions form a triangular lattice with a periodicity of 5.96 Å, and the primitive vector **a** is aligned along the armchair direction of NbSe₂ (see Fig. S3). To simplify the latter discussion, we define orthometric **x-y** coordinates (as labelled in Fig. 1b) such that **y** is parallel to vector **a** and **x** is defined along the armchair (zigzag) direction of the triangular lattice of oval protrusions (NbSe₂). An atomically resolved image (Fig. 1c), acquired under a smaller bias of -0.35 V, reveals that one oval

protrusion is composed of three top-layer Cl atoms (labelled Cl-1, Cl-2, and Cl-3). Most intriguingly, atoms Cl-1 to Cl-3 form a boomerang-like structure, rather than a linear one, where the middle Cl-2 atom protrudes in the $+y$ direction. In addition, the Cl-2 atom is approximately 0.05 Å higher than the other two Cl atoms in the z direction, as illustrated in a close-up 3D perspective plot (upper panel in Fig. 1d).

Our DFT calculations reproduce this unusual morphology observed in STM. Figure 1e shows a schematic model of a free-standing pristine VCl_3 ML, while Fig. 1f illustrates the fully relaxed atomic structure of the most energetically favoured stacking configuration of the VCl_3 ML grown on NbSe_2 (see the detailed discussion in Fig. S4). Upon stacking on NbSe_2 , the out-of-plane (OOP) inversion symmetry is lifted. In addition, the IP C_3 rotational symmetry is also broken owing to interfacial interactions (as elucidated later) that appreciably distort the V-Cl_6 octahedra. For clearer visualization, the lattice distortions are slightly exaggerated in Fig. 1e. Such distortion shifts the top-layer Cl atoms off their original positions, allowing us to identify the experimentally defined Cl-1 to Cl-3 atoms in the theoretical model (Fig. 1d and 1f). The middle Cl-2 atom sits higher than the Cl-1 and Cl-3 atoms by 0.02 Å in the calculations (0.05 Å in the experiments), and there is indeed a lateral shift of the Cl-2 atom in the $+y$ direction, forming an IP boomerang-like arrangement. The validity of the theoretical model is further verified by a one-to-one comparison of simulated and experimental constant- I STM images (Fig. 1g), while the detailed mechanism for the formation of this distorted structure on NbSe_2 will be discussed later.

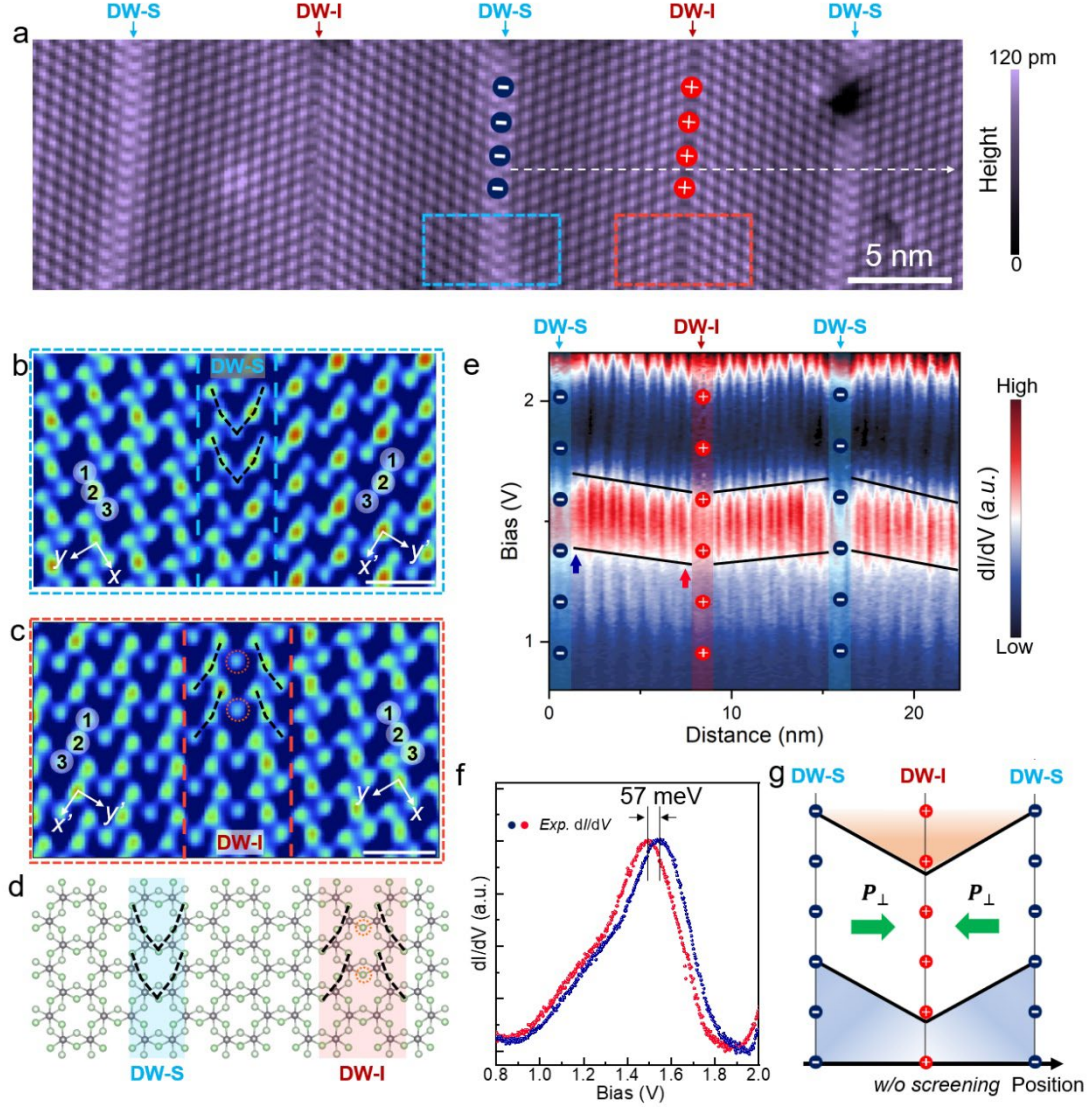


Figure 2 | IP electric polarizations characterized by band bending near DWs. **a**, STM image of a series of parallel domains of ML-VCl₃ on a NbSe₂ substrate. Scanning parameters: $V_b = 1.5$ V, $I_t = 100$ pA, and scale bar: 5 nm. Two types of DWs are denoted DW-I and DW-S. The “+” and “-” signs on DW-I and DW-S indicate positive and negative polarization charges, respectively. **b** and **c**, Atomically resolved STM images of DW-S and DW-I (the blue and red rectangles in **a**), respectively. $V_b = -0.35$ V, $I_t = 50$ pA, and scale bar: 1 nm. The numbers 1, 2, and 3 follow the definitions in Fig. 1c. The black boomerang-like polygonal lines represent the Cl trimers. The red circles in **c** mark the isolated Cl atoms in DW-I. The x (x')- y (y') coordinates are defined to show the different orientations of the two neighbouring domains, with x (x') along the armchair direction of the triangular lattice of oval protrusions, as we defined in Fig. 1b. Blue and red dashed lines were added as guides to the eyes. **d**, Schematic model of DW-S/I. Cl boomerangs sharing Cl atoms in DW-S and isolated Cl atoms in DW-I are marked. **e**, Spatially resolved dI/dV spectra acquired along the white dashed arrow in **a**. The feedback loop opened at $V_b = 2.2$ V, $I_t = 200$ pA, and lock-in modulation $V_{rms} = 6$ mV. The shadowed regions with “+” and “-” markers indicate the positions of the corresponding DWs. **f**, Two selected dI/dV spectra taken at the arrows labelled in **e** (plotted with the corresponding colours, dotted). **g**, Schematic model of the IP electric-polarization-induced band bending without a screening effect. The net charges on DW-S

(negative) and DW-I (positive) are marked as shown. The green arrows and P_{\perp} denote the components of the polarization vector perpendicular to the DWs.

Figure 2a shows a magnified image of the VCl_3 flake shown in Fig. 1a, which exhibits a series of parallel boundaries. Two types of domain walls (DWs) were distinguished under a scanning bias of $V_b = 1.5$ V, showing alternating bright (DW-S) and dark (DW-I) DWs. Figures 2b and 2c show atomically resolved STM images of DW-S and DW-I, respectively. At DW-S, two adjacent Cl boomerangs share a common Cl atom (Fig. 2d), while at DW-I, an isolated Cl atom separates two adjacent Cl boomerangs. The topology of the atomic lattice is continuous across both DW-S and DW-I (see Fig. S5 for details), excluding the possibility of dislocation defects. In addition, the lattice distortions, which are characterized by the $+y$ directions of Cl boomerangs, as labelled in Figs. 2b and 2c, are always mirror symmetric in the adjacent domains, and DW-S and DW-I correspond to the tail-to-tail and head-to-head configurations of the $+y$ coordinates. For simplicity, we used these parallelly aligned DWs in the following discussion, although they are not necessarily parallel, as the lattice distortion is six-fold degenerate in ML- VCl_3 (Fig. S6).

The alternating bright and dark topographic contrasts of DWs (Fig. 2a) suggest spatial variations in the local density of states across the DWs. Figure 2e shows a colour-coded rendering of the band mapping taken along a pathway across three DWs (white dashed line in Fig. 2a). We used the conduction band, sitting approximately 1.5 eV above the Fermi level, for illustration, which is more evident than the valence band, to show the spatial variation in electronic states (Fig. S2). Clear band bending was observed within each domain. The energy level of the energy band, *i.e.*, the ~ 1.5 eV

conduction band, near DW-S is always higher than that near DW-I. An energy shift of 57 meV was determined by comparing two selected spectra extracted near DW-S and DW-I (Fig. 2f). This band bending suggests that DW-S and DW-I are most likely negatively and positively charged. Figure 2g shows a schematic summarizing the charge accumulation and band bending at the DWs. The band bending does not show apparent dielectric screening effects³, ascribed to the relatively narrow domains here. In Fig. S7, we show that substantially different band bending behaviours are also observable between opposite edges of the ML-VCl₃ flakes²⁹. These lattice-deformation-linked changes in the charge polarities at DWs and/or edges were widely adopted in previous STM studies to recognize IP electric polarizations in 2D layers^{3,29,30}.

Moreover, in an STM set-up, the applied bias voltage between the conductive tip and a sample gives rise to a local electric field with an IP component³¹. Under given tunnelling conditions, this IP component of the applied electric field could reversibly switch the direction of the local IP electric polarization in ML-VCl₃, causing controllable movement of DWs (see Fig. S8 for details). This net electric polarization and the associated external-field-controlled manipulation of its direction are two criteria widely adopted in previous STM studies to justify the existence of FE order^{3,29,32}. In terms of the FE polarization vector \mathbf{P} , our STS measurements can only reveal the component perpendicular to the DWs, namely, \mathbf{P}_\perp , which was experimentally derived to be $\sim 0.04 \mu\text{C}\cdot\text{cm}^{-2}$ (see Methods for details). This polarization strength is comparable to that of known FE vdW layers, such as bilayer WTe₂ ($\sim 0.19 \mu\text{C}\cdot\text{cm}^{-2}$)³³ and twisted bilayer graphene/hBN ($\sim 0.1 \mu\text{C}\cdot\text{cm}^{-2}$)³⁴.

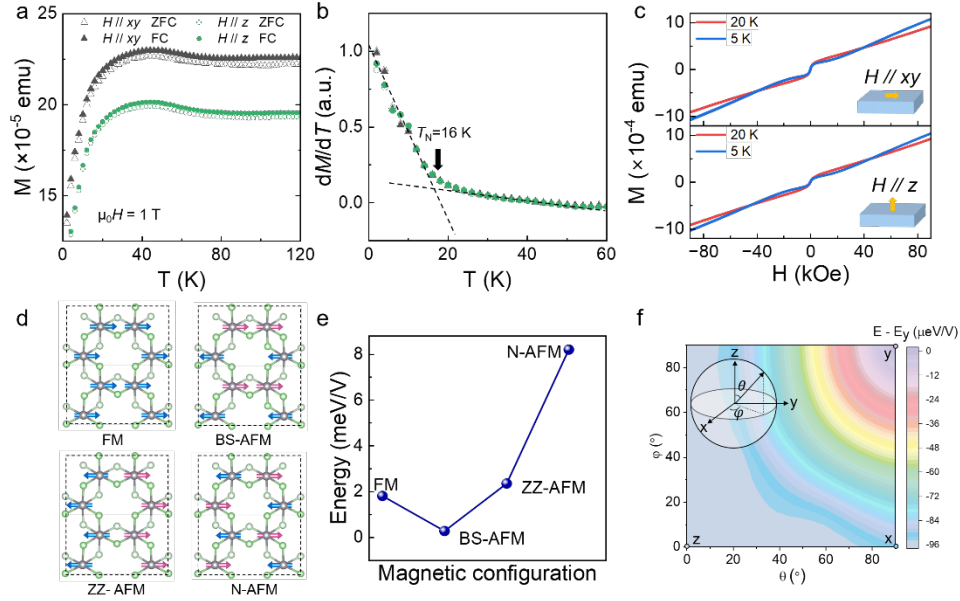


Figure 3 | Experimental and theoretical investigations of the magnetic order in epitaxy ML-VCl₃. **a**, M - T curves taken under IP (black) and OOP (green) magnetic fields ($H = 1$ T). ZFC and FC data are shown as hollow and solid dots, respectively. **b**, dM/dT data for determining the AFM transition temperature T_N . **c**, Upper (lower) panels show M - H curves taken under IP (OOP) magnetic fields. The red and blue curves correspond to the magnetization curves acquired at temperatures above and below T_N (*i.e.*, 20 K and 5 K, respectively). The details are shown in Fig. S12. **d**, Illustrations of the ferromagnetic (FM), bistriped (BS), zigzag (ZZ), and Néel (N) AFM configurations of ML-VCl₃ on NbSe₂. The NbSe₂ lattice is not displayed for simplicity. The green and grey balls represent Cl and V atoms, respectively. **e**, Plot of total energies for the four magnetic configurations. **f**, Magnetic anisotropy energy mapping of ML-VCl₃ on NbSe₂ with a bistriped AFM configuration. The coordinate system was defined as shown. The energy of the magnetic moment in the y direction (E_y) is set as the zero-point energy.

Next, we performed VSM measurements to investigate the magnetic properties of this FE VCl₃ ML (details are discussed in the Methods section and Figs. S9-11). The magnetization-temperature (M - T) curves are plotted in Fig. 3a for both zero-field cooling (ZFC) and field cooling (FC) procedures, in which the maximum magnetic field ($\mu_0 H$) reached 1 T. Both M - T curves coincide well with each other. An AFM order was characterized by a rapid decrease in magnetization (M) with a decrease in temperature (T) to below the transition temperature T_N . The T_N value was subsequently determined to be $T_N=16$ K by extracting the linear onset of the dM/dT curve (Fig. 3b), which is

close to the AFM transition temperature of 20 K for bulk VCl_3 ^{21,23}. The M - H measurements (Fig. 3c) further support the discovered AFM order^{35,36}, despite the weak ferromagnetic (FM) features observed near the zero-field region (details are shown in Figs. S10 and S11). In previous studies^{37,38}, similar FM features were ascribed to the graphene substrates used for VSM measurements, which were also observed in our measurements on bare graphene substrates (see detailed discussion in Fig. S10). For all our measurements, the magnetization-field curves show similar features for both the IP and OOP magnetic fields, indicating canted magnetic moments in the AFM VCl_3 MLs. Theoretically, we considered four typical magnetic orders for NbSe_2 -supported ML- VCl_3 , as displayed in Fig. 3d, the total energies of which are plotted in Fig. 3e. The bistriped AFM (BS-AFM) order is at least 2 meV more stable than the other orders. The magnetic moments of the BS-AFM configuration preferably orient in the x - z easy plane, exhibiting a negligible (0.005 meV/ VCl_3) energy difference within the plane (Fig. 3f), while rotating the moments to the y -axis increases the total energy by 0.10 meV/ VCl_3 . The magnetic anisotropy revealed by DFT is well consistent with the VSM results. All these results indicate that BS-AFM order with an x - z easy plane formed in our ML- VCl_3 . Our theoretical calculations also indicate that the preferred magnetic configuration is strongly correlated with the atomic structure deformations and their induced electric polarizations (see Fig. S12 for details). This close connection implies coupled spin and electric orders in ML- VCl_3 , which is a key characteristic of a type-II multiferroic material.

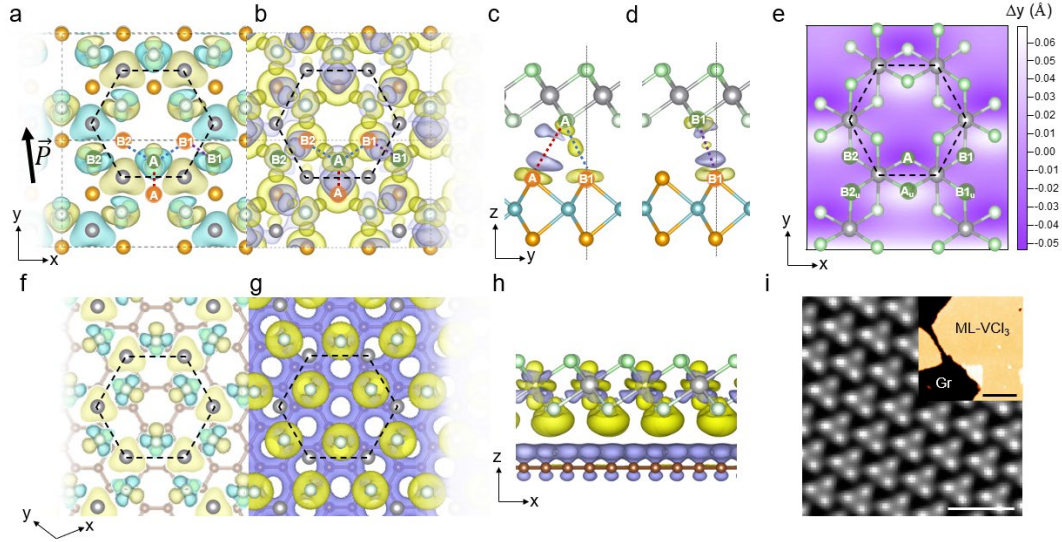


Figure 4 | Anisotropic charge-transfer-induced IP ferroelectricity and comparison with the VCl_3 -graphene interface. **a**, Top view of the spin density at the VCl_3 - NbSe_2 interface. Only V atoms, top-layer Se atoms, and bottom-layer Cl atoms are shown. The V, Se, and Cl atoms are shown in grey, orange, and light green, respectively. The red (white) letters mark Cl (Se) atoms A-B. The yellow (blue) isosurface represents spin up (down), and an isosurface value of $1.2 \times 10^{-4} e/\text{bohr}^3$ was used. The black arrow in **a** indicates the polarization direction \vec{P} . **b**, Top view of the DCD at the VCl_3 - NbSe_2 interface. A yellow (purple) isosurface represents charge accumulation (reduction). The blue dashed lines represent Coulomb repulsion, and the red dashed line represents Coulomb attraction. **c**, **d**, Side views of DCDs at the VCl_3 - NbSe_2 interface solely along path Cl_A-Se_A (red dashed line), Cl_A-Se_B1 (blue dashed line) (**c**) or Cl_B1-Se_B1 (violet dashed line) (**d**). **e**, Atomic displacements in the y direction in NbSe_2 -supported VCl_3 . The displacements were extracted with respect to the pristine atomic structure. Top (bottom)-layer Cl atoms are marked by A_u (A), $B1_u$ (B1), and $B2_u$ (B2). **f**, **g**, Top view of the spin density and DCD at the VCl_3 -graphene interface. **h**, Side view of the DCD at the VCl_3 -graphene interface. An isosurface value of $3 \times 10^{-4} e/\text{bohr}^3$ was used. Carbon atoms are shown in brown. **i**, Atomically resolved STM image of ML- VCl_3 grown on a graphene/SiC substrate ($V_b = 0.5$ V, $I_t = 50$ pA, and scale bar: 1 nm). The inset shows a large-area image, where Gr represents the graphene substrate ($V_b = 1.5$ V, $I_t = 20$ pA, and scale bar: 20 nm).

We next discuss the most likely origin(s) of the associated IP ferroelectricity. The preferred BS-AFM configuration results in two types of interfacial Cl atoms, namely, Cl_A and Cl_B1 (Cl_B2), denoted by the green background white letters A and B1 (B2) in the spin-density plot shown in Fig. 4a. Atom Cl_A is sandwiched by two spin-density contours of the same component (yellow isosurface) and lacks spin density in the

positive y direction. However, the two-neighbouring spin-density contours of atom Cl_B1 (Cl_B2) are in different spin components (one yellow and one blue isosurface).

This unbalanced spin-density distribution breaks the IP C_3 rotational symmetry of the VCl_3 overlayer, which induces at least three categories of electron redistribution at the Cl-Se interfaces, as illustrated by the interfacial differential charge density (DCD) at the VCl_3 - $NbSe_2$ interface (Figs. 4b and 4c). An approximately y - z mirror plane could be identified from either the spin density (Fig. 4a) or the DCD (Fig. 4b), where interactions involving Cl_B1 and Se_B1 (orange background white letter B1 hereinafter) are nearly mirror symmetric with those involving Cl_B2 and Se_B2, respectively, e.g., Cl_A-Se_B1 is mirror symmetric with Cl_A-Se_B2. This mirror symmetry nearly eliminates likely IP electric polarization in the x direction. Along path Cl_A-Se_B1 (blue lines in Fig. 4b and 4c), only charge accumulation appears (Fig. 4c). However, directional charge reduction is primarily observed along path Cl_A-Se_A (denoted by the red lines in Figs. 4b and 4c), and alternating charge accumulation and reduction are found along path Cl_B1-Se_B1 (violet dashed line in Fig. 4d). These different charge variations at the Cl-Se interface potentially induce anisotropic atomic displacements for the interfacial Cl atoms and thus likely IP electric polarization in the y direction.

In Fig. 4e, we plot the colour-coded distribution of the atomic displacements in the y direction with respect to the pristine atomic structure of ML- VCl_3 . The enhanced electron density along path Cl_A-Se_B1 (Fig. 4c) pulls these two atoms away from each other, while the alternating charge accumulation and reduction provide relatively

more attractive interactions between Cl_A and Se_A (Cl_{B1} and Se_{B1}). Therefore, the overall result leads to Cl_A undergoing a negative displacement (darkest area in Fig. 4e) and Cl_{B1} (Cl_{B2}) undergoing a slightly positive shift (brighter areas in Fig. 4e) relative to the *y*-axis. As the structures of interfacial and surface Cl atoms are locked by the V-Cl₆ octahedron, the surface Cl atoms are shifted upwards for A_u (brightest area in Fig. 4e) and moved slightly downwards for B1_u and B2_u (darker areas) in the *y* direction, which were observed in our STM imaging and DFT simulations.

This nonsymmetric displacement field of cations/anions leads to an ionic contribution of (-0.063, 0.072) $\mu\text{C}\cdot\text{cm}^{-2}$ to the (*x,y*) vector of the electric polarization. This ionic polarization is well screened, particularly in the *x* direction, by electrons within the ML-VCl₃, for which the calculated electronic contribution is (0.060, -0.055) $\mu\text{C}\cdot\text{cm}^{-2}$, which largely reduces the IP polarization to (-0.002, 0.017) $\mu\text{C}\cdot\text{cm}^{-2}$. Interfacial electrons distribution from the substrate further slightly screens this polarization and suppress it to (-0.003, 0.014) $\mu\text{C}\cdot\text{cm}^{-2}$, which is on the same order of magnitude as the polarization estimated in our experiments. In brief, the IP polarization arises from incomplete electronic screening of the distorted VCl₃ overlayer, while the distortion is ascribed to the magnetism-induced breaking of the *C*₃ rotational symmetry, which is promoted by directional Cl–Se interfacial electronic interactions.

To verify the crucial role that the directional interaction plays in the IP electric polarization at the VCl₃-NbSe₂ vdW interface, we theoretically constructed a VCl₃ ML on a graphene substrate governed by nondirectional interfacial interactions³⁹. Analogous to Figs. 4a to 4d, the spin density, top view of the interfacial DCD and side

view of the interfacial DCD are plotted for the $\text{VCl}_3/\text{graphene}$ heterostructure in Figs. 4f to 4h, respectively. Both top views (Figs. 4f and 4g) indicate that the C_3 rotational symmetry is nearly maintained for VCl_3 on the graphene substrate, in which the FM order is most energetically favoured for the VCl_3 ML. While an OOP interface dipole forms at the VCl_3 -graphene interface (Fig. 4h), the induced IP charge variation is, unlike in the NbSe_2 case, isotropic and directionless (Fig. 4f and 4g). Similar isotropic IP interfacial interactions were previously observed at metal-graphene interfaces^{39,40}. In the present case, the heterojunction provides an OOP polarization of $-1.76 \mu\text{C}\cdot\text{cm}^{-2}$ and a nearly zero IP polarization. Controlled experiments were also performed via growth of a VCl_3 ML on a graphene/SiC substrate (see Methods for details of the growth). Figure 4i shows a typical STM image of ML- VCl_3 deposited on graphene/SiC, which indicates that the atomic structure, at least for the surface Cl atoms, is not appreciably distorted and exhibits no polarized domains or well-defined DWs, consistency with our calculated results of the $\text{VCl}_3/\text{graphene}$ heterostructure (see Fig. S13 for more details).

In conclusion, we observed both IP and OOP electric polarizations in a magnetic VCl_3 ML selectively grown on a NbSe_2 substrate. By combining STM, VSM, and first-principles calculations, we explicitly demonstrate the coexistence and coupling of IP ferroelectricity and canted bistriped antiferromagnetism. In addition to the broken inversion symmetry origin for the ferroelectricity, we found that the magnetism-induced breaking of the IP C_3 rotational symmetry leads to IP ferroelectricity and is strengthened by directional interfacial Cl-Se electronic interactions. In addition to the previously known inversion Dzyaloshinskii-Moriya interaction⁴¹, we found another route in which

antiferromagnetism could lead to ferroelectricity. Experiments and calculations for the VCl_3 -graphene interface verified this mechanism for introducing ferroelectricity, in which vdW interfacial interactions seem to play an elegant role in tailoring the crystalline symmetry and its related emergent quantum phases. Our findings not only provide a potential ML platform for MF but also refresh the understanding of vdW interface engineering in controlling functional polarizations through multiple degrees of freedom.

Methods

Sample preparations. The sample growth was carried out within a UHV-MBE system with a base pressure of $\sim 2.4 \times 10^{-10}$ Torr. High-quality VCl_3 powder (99.5%) was evaporated by a home-built Knudsen cell evaporator. The flux rate was measured to be ~ 0.15 ML/hour at a growth temperature of 523 K. A fresh NbSe_2 surface was acquired by cleaving a bulk NbSe_2 crystal in a UHV load-lock chamber at room temperature. During the growth of ML- VCl_3 on NbSe_2 , the substrate temperature was held at 420 K. Postannealing procedures were performed for one hour at 420 K to ensure high-quality crystallization. The growth of ML- VCl_3 on graphene and ML- NbSe_2 substrates involved growth parameters identical to those for growth on bulk NbSe_2 . Graphene layers were prepared on 4H-SiC(0001) wafers by a well-established method of vacuum annealing⁴². Single-layer or bilayer graphene could be selectively formed on the SiC(0001) surface by controlling the annealing time⁴². Single-layer graphene was used for direct VCl_3 deposition (the samples presented in Fig.4d and Fig. S13), and bilayer

graphene was used for preparing ML-NbSe₂ (*i.e.*, the substrates used in VSM measurements). ML 1H-NbSe₂ was grown on graphene/SiC following a previously reported method⁴³. High-quality Nb (99.5%) and Se (99.999%) were evaporated by an electron-beam evaporator and a home-built Knudsen cell evaporator, respectively. High-quality Nb (99.5%) and Se (99.999%) were evaporated by an electron-beam evaporator and a home-built Knudsen cell evaporator, respectively. The flux ratio between Nb and Se was ~1:20, while the substrates were held at 773 K during deposition. To protect the sample from degradation in air, 10 nm Se capping layers were deposited on ML-VCl₃ before moving it from the ultrahigh vacuum environment to perform VSM measurements.

STM/STS and VSM measurements. The STM/STS measurements were carried out on a commercial Unisoku-1300 system. All the measurements were taken at the liquid helium temperature (~ 4.3 K). The PtIr tips used in this work were calibrated by measuring the surface state of a Cu (111) crystal. Tunnelling spectroscopies were performed by utilizing a standard lock-in amplifier with a modulation frequency of 932 Hz. The modulation voltages used are specified in the figure captions. STM images were processed using *Gwyddion*⁴⁴. Magnetic susceptibility measurements were performed in the Quantum Design PPMS DynaCool with a VSM option. To enhance the signal strength, we stacked 12 pieces of 2 × 2 mm² ML-VCl₃/NbSe₂ samples together. ZFC and FC measurements were performed in both in-plane and out-of-plane directions at 1 T, covering a temperature range from 2 to 390 K with increments of 2 K

for each step. Magnetization measurements were carried out by sweeping the magnetic field from -9 to 9 T at various temperatures.

DFT calculations. Calculations were performed using the generalized gradient approximation in the Perdew–Burke–Ernzerhof (PBE) form⁴⁵ for the exchange–correlation potential, the projector augmented wave method⁴⁶, and a plane–wave basis set as implemented in the Vienna ab initio simulation package (VASP)⁴⁷. Grimme’s D3 form vdW correction was considered with the PBE exchange functional (PBE-D3)⁴⁸ in all structural relaxations. On-site Coulomb interactions of the V *d* orbitals were considered using a DFT+U method⁴⁹ with $U= 3$ eV, consistent with the values used in the literature^{17,26,50}. The structures were fully relaxed until the residual force per atom was less than 0.005 eV/Å. A plane-wave energy cutoff of 450 eV was adopted for the structural relaxation calculation. A k-mesh of $7\times 13\times 1$ ($5\times 5\times 1$) was used to sample the first Brillouin zone of VCl₃ on NbSe₂ (graphene). All the vacuum layers adopted (>15 Å) were sufficient to appreciably reduce the image interactions. A $\sqrt{3}\times 1$ rectangular lattice (2×2 hexagonal lattice) was adopted for VCl₃ on NbSe₂ (graphene). Two-layer NbSe₂ (graphene) was used to model the substrate, in which the bottom layer was kept fixed and the top layer was allowed to fully relax. Atomic position projections were obtained by subtracting the corresponding atomic positions of bare VCl₃ with inversion symmetry from the structure of VCl₃ relaxed on NbSe₂. Electric polarizations were derived using the Berry phase method⁵¹.

Experimental estimation of the polarization. By taking the two nearby DWs and the area between them as a parallel-plate capacitor filled with a homogeneous dielectric,

the IP polarization could be calculated by the equation $P = (\varepsilon_r - 1)\varepsilon_0 V/d$, where ε_r is the relative permittivity of VCl_3 , ε_0 is the electric constant, and V/d is the electric field, in which V and d are the maximum energy shift and the corresponding distance between the two opposite neighbouring DWs⁵². Since the ε_r of VCl_3 is unknown, we took the value for CrCl_3 ($\varepsilon_r = 8$) in our approximation calculations⁵³.

Reference

1. Gong, C. *et al.* Discovery of intrinsic ferromagnetism in two-dimensional van der Waals crystals. *Nature* **546**, 265–269 (2017).
2. Huang, B. *et al.* Layer-dependent ferromagnetism in a van der Waals crystal down to the monolayer limit. *Nature* **546**, 270–273 (2017).
3. Chang, K. *et al.* Discovery of robust in-plane ferroelectricity in atomic-thick SnTe. *Science* **353**, 274–278 (2016).
4. Fei, Z. *et al.* Ferroelectric switching of a two-dimensional metal. *Nature* **560**, 336–339 (2018).
5. Qi, J., Wang, H., Chen, X. & Qian, X. Two-dimensional multiferroic semiconductors with coexisting ferroelectricity and ferromagnetism. *Appl. Phys. Lett.* **113**, 043102 (2018).
6. Xu, M. *et al.* Electrical Control of Magnetic Phase Transition in a Type-I Multiferroic Double-Metal Trihalide Monolayer. *Phys. Rev. Lett.* **124**, 067602 (2020).
7. Zhang, J.-J. *et al.* Type-II Multiferroic Hf₂VC₂F₂ MXene Monolayer with High Transition Temperature. *J. Am. Chem. Soc.* **140**, 9768–9773 (2018).
8. Song, Q. *et al.* Evidence for a single-layer van der Waals multiferroic. *Nature* **602**, 601–605 (2022).
9. Jiang, Y. *et al.* Dilemma in optical identification of single-layer multiferroics. *Nature* **619**, E40–E43 (2023).
10. Wu, S. *et al.* Layer thickness crossover of type-II multiferroic magnetism in C. Preprint at <https://doi.org/10.48550/arXiv.2307.10686> (2023).
11. Miao, M.-P. *et al.* Spin-resolved imaging of atomic-scale helimagnetism in monolayer NiI₂. Preprint at <https://doi.org/10.48550/arXiv.2309.16526> (2023).
12. Amini, M. *et al.* Atomic-Scale Visualization of Multiferroicity in Monolayer NiI₂. *Adv. Mater.* 2311342 (2024) doi:10.1002/adma.202311342.
13. Ju, H. *et al.* Possible Persistence of Multiferroic Order down to Bilayer Limit of van der Waals Material NiI₂. *Nano Lett.* **21**, 5126–5132 (2021).
14. Liu, N. *et al.* Competing Multiferroic Phases in NiI₂ Mono- and Few-layers. Preprint at <https://doi.org/10.48550/arXiv.2211.14423> (2023).
15. Song, L. *et al.* Robust multiferroic in interfacial modulation synthesized wafer-scale one-unit-cell of chromium sulfide. *Nat. Commun.* **15**, 721 (2024).
16. Huang, C. *et al.* Prediction of Intrinsic Ferromagnetic Ferroelectricity in a Transition-Metal Halide Monolayer. *Phys. Rev. Lett.* **120**, 147601 (2018).
17. Huang, C., Wu, F., Yu, S., Jena, P. & Kan, E. Discovery of twin orbital-order phases in ferromagnetic semiconducting VI₃ monolayer. *Phys. Chem. Chem. Phys.* **22**, 512–517 (2020).
18. Son, S. *et al.* Bulk properties of the van der Waals hard ferromagnet VI₃. *Phys. Rev. B* **99**, 041402(R) (2019).
19. Kong, T. *et al.* VI₃—a New Layered Ferromagnetic Semiconductor. *Adv. Mater.* **31**, 1808074 (2019).
20. Tian, S. *et al.* Ferromagnetic van der Waals Crystal VI₃. *J. Am. Chem. Soc.* **141**, 5326–5333 (2019).
21. Kratochvilova, M. *et al.* Crystal structure evolution in the van der Waals vanadium trihalides. *J. Phys. Condens. Matter* **34**, 294007 (2022).

22. Lyu, B. *et al.* Structural and magnetic phase transitions in quasi-two-dimensional VBr₃. *Phys. Rev. B* **106**, 085430 (2022).
23. Mastrippolito, D. *et al.* Polaronic and Mott insulating phase of layered magnetic vanadium trihalide VCl₃. *Phys. Rev. B* **108**, 045126 (2023).
24. De Vita, A. *et al.* Influence of Orbital Character on the Ground State Electronic Properties in the van Der Waals Transition Metal Iodides VI₃ and CrI₃. *Nano Lett.* **22**, 7034–7041 (2022).
25. Lin, Z. *et al.* Magnetism and Its Structural Coupling Effects in 2D Ising Ferromagnetic Insulator VI₃. *Nano Lett.* **21**, 9180–9186 (2021).
26. He, J., Ma, S., Lyu, P. & Nachtigall, P. Unusual Dirac half-metallicity with intrinsic ferromagnetism in vanadium trihalide monolayers. *J. Mater. Chem. C* **4**, 2518–2526 (2016).
27. Chen, W. *et al.* Direct observation of van der Waals stacking–dependent interlayer magnetism. *Science* **366**, 983–987 (2019).
28. Li, P. *et al.* Single-layer CrI₃ grown by molecular beam epitaxy. *Sci. Bull.* **65**, 1064–1071 (2020).
29. Zhang, Z. *et al.* Atomic Visualization and Switching of Ferroelectric Order in β -In₂Se₃ Films at the Single Layer Limit. *Adv. Mater.* **34**, 2106951 (2022).
30. Huo, D. *et al.* Tuning of the Valley Structures in Monolayer In₃Se₃/WSe₂ Heterostructures via Ferroelectricity. *Nano Lett.* **22**, 7261–7267 (2022).
31. Chang, K. *et al.* Microscopic Manipulation of Ferroelectric Domains in SnSe Monolayers at Room Temperature. *Nano Lett.* **20**, 6590–6597 (2020).
32. Gou, J. *et al.* Two-dimensional ferroelectricity in a single-element bismuth monolayer. *Nature* **617**, 67–72 (2023).
33. Fei, Z. *et al.* Ferroelectric switching of a two-dimensional metal. *Nature* **560**, 336–339 (2018).
34. Zheng, Z. *et al.* Unconventional ferroelectricity in moiré heterostructures. *Nature* **588**, 71–76 (2020).
35. Kong, T., Guo, S., Ni, D. & Cava, R. J. Crystal structure and magnetic properties of the layered van der Waals compound VBr₃. *Phys. Rev. Mater.* **3**, 084419 (2019).
36. Wildes, A. R., Simonet, V., Ressouche, E., Ballou, R. & McIntyre, G. J. The magnetic properties and structure of the quasi-two-dimensional antiferromagnet CoPS₃. *J. Phys. Condens. Matter* **29**, 455801 (2017).
37. Wang, Y. *et al.* Room-Temperature Ferromagnetism of Graphene. *Nano Lett.* **9**, 220–224 (2009).
38. Červenka, J., Katsnelson, M. I. & Flipse, C. F. J. Room-temperature ferromagnetism in graphite driven by two-dimensional networks of point defects. *Nat. Phys.* **5**, 840–844 (2009).
39. Huang, Y. *et al.* Universal mechanical exfoliation of large-area 2D crystals. *Nat. Commun.* **11**, 2453 (2020).
40. Fu, Q. *et al.* One-Step Exfoliation Method for Plasmonic Activation of Large-Area 2D Crystals. *Adv. Sci.* **9**, 2204247 (2022).
41. Cheong, S.-W. & Mostovoy, M. Multiferroics: a magnetic twist for ferroelectricity. *Nat. Mater.* **6**, 13–20 (2007).
42. Wang, Q. *et al.* Large-scale uniform bilayer graphene prepared by vacuum graphitization of 6H-SiC(0001) substrates. *J. Phys. Condens. Matter* **25**, 095002 (2013).
43. Wan, W. *et al.* Observation of Superconducting Collective Modes from Competing Pairing Instabilities in Single-Layer NbSe₂. *Adv. Mater.* **34**, 2206078 (2022).

44. Nečas, D. & Klapetek, P. Gwyddion: an open-source software for SPM data analysis. *Open Phys.* **10**, 181–188 (2012).
45. Perdew, J. P., Burke, K. & Ernzerhof, M. Generalized gradient approximation made simple. *Phys. Rev. Lett.* **77**, 3865–3868 (1996).
46. Blöchl, P. E. Projector augmented-wave method. *Phys. Rev. B* **50**, 17953–17979 (1994).
47. Kresse, G. & Furthmüller, J. Efficient iterative schemes for *ab initio* total-energy calculations using a plane-wave basis set. *Phys. Rev. B* **54**, 11169–11186 (1996).
48. Grimme, S., Antony, J., Ehrlich, S. & Krieg, H. A consistent and accurate *ab initio* parametrization of density functional dispersion correction (DFT-D) for the 94 elements H-Pu. *J. Chem. Phys.* **132**, 154104 (2010).
49. Anisimov, V. I., Aryasetiawan, F. & Lichtenstein, A. I. First-principles calculations of the electronic structure and spectra of strongly correlated systems: the LDA+ U method. *J. Phys. Condens. Matter* **9**, 767 (1997).
50. Yekta, Y. *et al.* Strength of effective Coulomb interaction in two-dimensional transition-metal halides MX_2 and MX_3 ($M = \text{Ti}, \text{V}, \text{Cr}, \text{Mn}, \text{Fe}, \text{Co}, \text{Ni}$; $X = \text{Cl}, \text{Br}, \text{I}$). *Phys. Rev. Mater.* **5**, 034001 (2021).
51. King-Smith, R. D. & Vanderbilt, D. Theory of polarization of crystalline solids. *Phys. Rev. B* **47**, 1651–1654 (1993).
52. Feynman, R. P., Leighton, R. B. & Sands, M. *The Feynman Lectures on Physics, Vol. II: The New Millennium Edition: Mainly Electromagnetism and Matter*. (Basic Books, 2011).
53. Borghesi, A., Guizzetti, G., Marabelli, F., Nosenzo, L. & Reguzzoni, E. Far-infrared optical properties of CrCl_3 and CrBr_3 . *Solid State Commun.* **52**, 463–465 (1984).

Acknowledgments

We thank the supports from the National Key R&D Program of China (Grant No. 2023YFA1406500, 2018YFA0703700), the National Natural Science Foundation of China (Grant No. 11974012 and 12134011), the Strategic Priority Research Program of Chinese Academy of Sciences (No. XDB30000000), the Fundamental Research Funds for the Central Universities, China, and the Research Funds of Renmin University of China [22XNKJ30 (W.J.)]. D.P.G. was supported by the Outstanding Innovative Talents Cultivation Funded Programs 2023 of Renmin University of China. Calculations were performed at the Physics Lab of High-Performance Computing and the Public Computing Cloud, Renmin University of China.

Author Contributions

J.H.D. and S.Z.L. prepared the samples, and carried out the STM/STS measurements and the data analysis. D.P.G. and W.J. performed the first-principles calculations. Y.W. performed the VSM measurements under the supervision of J.H.. Z.B.C, Z.M.P., T.J., and Y.S.B. contributed to the sample preparations. Z.B.C. and H.Z. contributed to the STM measurements. C.D.Z. initiated the work, advised on the experiments, and provided input on the data analysis. W.J. conceived the theoretical calculations and analysis. J.H.D., D.P.G., Y.W., W.J., and C.D.Z. wrote the manuscript with input from the co-authors.

Competing interests

The authors declare no competing interests.

Additional information

Supplementary information is available for this paper at XXX.